*International Journal of Microwave and Wireless Technologies*

**cambridge.org/mrf**

# Wideband design and modeling of efficient multi-resonance reflective linear-to-circular polarization converter

Reza Zaker and Farid Jolani

Department of Electrical Engineering, Azarbaijan Shahid Madani University, Tabriz, Iran

**Research Paper**

**Cite this article:** Zaker R, Jolani F (2024) Wideband design and modeling of efficient multi-resonance reflective linear-to-circular polarization converter. *International Journal of Microwave and Wireless Technologies* **16**(7), 1096–1105. https://doi.org/10.1017/S1759078723001629

Received: 03 October 2023
Revised: 02 December 2023
Accepted: 11 December 2023

**Keywords:**
angular stability; axial ratio (*AR*); frequency-selective structure (FSS); linear-to-circular polarization converter; wideband converter

**Corresponding author:** Reza Zaker;
Email: zaker@azaruniv.ac.ir

## Abstract

A reflective linear-to-circular polarization converter based on dual frequency-selective structures (FSSs) is proposed and modeled to exhibit efficient wideband performance. The design utilizes a diagonal array of two connected circular patches as an effective anisotropy with regular current distribution in several successive resonances, resulting in orthogonal reflections with a 90° phase difference. The relevant upper-part characteristic is improved by using two separate square patches as a high-frequency resonator. This design with distinct key parameters leads to high overlapping and then excellent bandwidth and efficiency over 105% and 96%, respectively, with an axial ratio below 1.7 dB. A sophisticated equivalent circuit-admittance model including effective mutual coupling between two FSSs is extracted, featuring closed-form equations for the physical design. Different dielectric constants are studied on the converter, which offer controllable coverage in the range of 3–24 GHz (S, C, X, Ku, and K bands), variably. For actual validation, a very thin ($0.04\lambda_0$ at 3.65 GHz) 8 × 8 array prototype was built and measured at different incident angles, showing angular stability up to 45° in 78% (6–14 GHz) bandwidth. This converter has potential applications in communication, spectroscopy, detection, and imaging in micro-, mm-, and THz-wave regions.

## Introduction

Utilizing a polarization converter presents a distinct and advantageous approach to convert linearly polarized (LP) waves into circularly polarized (CP) waves and LP into LP waves, offering benefits across a wide range of frequencies, including microwave, terahertz (THz), and optical regions, in both reflective [1–4] and transmissive [5–10] modes of operation. Recent studies have shown that the most effective design for these converters involves applying metasurfaces and frequency-selective structure (FSS) with 2D and 3D [11] structures in one or more layers format. This approach increases the degree of design freedom and improves key characteristics, such as conversion bandwidth, conversion efficiency, and high angle stability. Converting LP into LP polarizations is crucial in many practical scenarios, such as radar cross-section reduction [12–15] and high-resolution imaging [16]. However, due to unique characteristics of CP and the high-tech demands of telecommunications industries, we will focus on it here. By employing circular polarization, which is less susceptible to multipath fading and Faraday rotation; satellite communication channels are isolated, frequency reuse is enabled, channel capacity is improved, interrogation range is increased in radio frequency identification (RFID) tags, and line-of-sight clutter is mitigated in indoor communication [17–20].

In an LP–CP converter, after the incident LP wave is split into two orthogonal in-phase LP waves and then reflected or transmitted by the converters, two field components will be operated with the same amplitude and 90° phase difference and finally superimposed into the CP wave [17]. According to primary research, an LP–CP converter is designed as a multi-layer FSS including cross-shaped slots [6, 21], capacitive patches and inductive wire grids [7], meander lines and strips [22, 23], meandered slots [24], and split rings [25] with inductive and capacitive properties to introduce a 90° phase shift between reflected/transmitted orthogonal polarizations, resulting in a CP wave. Recent studies have explored ways to improve the limited 3 dB-axial ratio (*AR*) bandwidth of traditional CP antennas by integrating a wideband LP antenna/array and wideband LP–CP converter [2, 18–20, 26–28]. In addition, there has been a focus on enhancing the angular stability of antenna-integrated converters for beamforming, sensing, and space applications [2, 20]. In [20], split rings and metallic strips were used on both sides of dielectric substrate to maintain stable characteristics of CP antenna array under transverse electric (TE) polarization up to an oblique incidence of 60°, but with a limited 3 dB-*AR* bandwidth of less than 10%. A Vivaldi antenna array achieved oblique incidence stability up to 30° and a wide CP bandwidth of 46% using a polygon-based anisotropic impedance surface as a reflective LP–CP converter [2]. In all aforementioned applications, reflective LP–CP

converter can provide better efficiency because of total reflection by metal ground [17, 19]. Many studies in this regard clarify that the key targets of these reflective converters are to design their phase characteristics within the interested wide 3 dB-*AR* band along with high angular stability. Recently, a 3D THz reflective LP–CP converter was proposed with a wide 1.98–4.12 THz (about 70%) CP bandwidth due to the overlaps of stronger electric and magnetic dipolar coupling resonances [11]. Furthermore, oblique incidence stability was achieved up to 50° in [29], by using split square ring as polarization converter and additional nested square patch as *AR* quality improver, while its CP bandwidth is less than 38%. To cover both wide LP–CP conversion and wide angular stability, a generalized design guideline was recently introduced in [2], using the admittance analysis of the equivalent circuit model (ECM) and admittance extraction through the area moment of inertia equations. The study in [3] proves that a symmetrical metasurface generates equal reflective orthogonal waves, resulting in high-quality and wideband circular polarization of over 90%. Along with the conversion bandwidth of 39%, angular stability up to 45° is achieved in a range of 10.1–15 GHz, using an arrow-linked figure of eight-square loop FSS in [30]. The same authors increased the bandwidth to 50% using a meander-line inductor separated by orthogonal dipoles in [31], maintaining the angular stability. In a study conducted recently [4], researchers utilized an open ring as dual resonator and a square patch as *AR* improver to attain 45° angular stability over two broad CP bands.

Despite the numerous research efforts in this area, the development of LP–CP converter with exceptional bandwidth, high efficiency, simple structure, and acceptable angular stability remains a significant challenge. This paper aims to tackle these challenges by focusing on the design of triple-layer dual multi-resonance FSS reflective LP–CP converter. A multi-resonator FSS in early and middle bands is made of connected circular patches, and a high-frequency single-resonator FSS is made of non-connected square patches. This combination creates multiple consecutive overlapping reflective resonances, resulting in a high-efficiency wide conversion band. An ECM and simultaneous step-by-step matrix analysis and simplification are presented, and finally, by using CP reflection conditions, closed-form equations are extracted for the physical design of both FSSs. The design is evaluated through detailed parametric studies, achieving a high conversion ratio or efficiency in the entire wide conversion band. The effects of different dielectric constants on conversion parameters are also analyzed, showing coverage of several standard bands from 4 to 22 GHz, variably. Hence, the coverage of different wide or narrow bands can be expected. Finally, an 8 × 8 array of the optimal cell of the converter is fabricated and measured, along with comparing and explaining the results. Furthermore, angular stability is also studied in the measurement process.

## Design and modeling the proposed reflective LP–CP converter

In this part, the structure, design, theory, ECM, and related properties are proposed.

### Configuration and design theory

The unit cell of the proposed reflective converter is shown in Fig. 1, including two FSS and three dielectrics, while the last layer is a purely metallic plane. The main reason for using FSSs in different layers is to create different resonant behavior for each and not to destroy each other. A frequency selective structure (FSS) with a circular shape can be assumed as a polygonal structure with many sides, which every side and discontinuity on the patch is assumed as a resonator. Moreover, the current distribution on circular patch is almost stable and uniform in most resonances (i.e., the main and harmonic ones). Thus, a circular patch can present multi-resonance behavior with successive positions. Hence, to create a multi-resonator with high degrees of freedom for flexible design, we introduce a two-element array of connected circular patches as the first FSS (i.e., FSS1) at the $h1$ position. As illustrated in top view, the relevant key parameters are *rc* and *dc*, which adjust the electrical length of the first reflective resonance, its harmonics, and their number. Hence, the position of the lower edge of the 3 dB-*AR* band and the number of resonances in the primary and middle bands will be controllable. According to the previous theory, the second FSS (i.e., FSS2) at $h1+h2$ height is defined as a two-element array of square patches separated from each other at the two ends of FSS1, so that, due to its single side and very small size, the single resonance in the high frequency of the band is created. The related key parameter is *ls*, which controls the position of the high resonance. Based on these two theories mentioned earlier, we will have two multi-resonance and single-resonance resonators cascaded, and a step-by-step parametric study on them will lead to the creation of a multi-resonance conversion band. Alternatively, we define three dielectric layers with the same dielectric constant but with different thicknesses, $h1$, $h2$, and $h3$ around the FSSs, so that the effective dielectric constant for all reflective resonances can be adjusted. Therefore the quality factor of the resonances can be also controlled. Finally, the frequency bandwidth of each one should be controlled. This number of design freedoms leads to the creation of successive resonances with full overlapping capability and ultimately creates a very wide conversion bandwidth with very low *AR*.

The initial value of all dielectric constants is equal to 2.2, with a loss tangent of 0.005. As shown in Fig. 1, the proposed cell of the converter is square and each side, as periodicity of the cell in the array, is equal to 10 mm. This value is smaller than the wavelength of the highest desired frequency in the band (i.e., 20 GHz) to ensure most higher-order Floquet modes are evanescent [2, 32].

### Circuit modeling, analysis, and discussion

As shown (side view) in Fig. 1, for the analysis and modeling of the cell, as a basic assumption, a TE-polarized (i.e., *y*-axis-directed wave) incident wave is assumed. As illustrated in Fig. 2(a) and considering $\vec{E}_i^y$ incident wave, the incident and reflected E fields can be readily decomposed into mutually orthogonal *u* and *v* components. The proposed dual-FSS cell is made diagonally symmetric to maximally decrease the coupling between the reflected *u* and *v* polarized waves. Therefore, the cross-polarized components of the reflected waves can be approached to zero, and then, the admittance matrix study on parallel cascaded ECM (Fig. 2(b)) will be significantly simplified [2, 29, 32]. This equivalent circuit is based on lumped network theory, and therefore, the ground plane in the last layer is modeled as a short circuit load, and all three dielectrics are modeled as a transmission line with certain characteristic admittance ($Y_d i$) and length ($h_i$), where $i = 1, 2, 3$. Two important points are included in this modeling, which are: (1) Use of frequency-dependent tensor sheet admittance for multi-resonance FSS1 (i.e., $Y_1(\omega)$) and another tensor sheet admittance for single-resonance FSS2 (i.e., $Y_2$). This admittance matrix is

https://doi.org/10.1017/S1759078723001629 Published online by Cambridge University Press

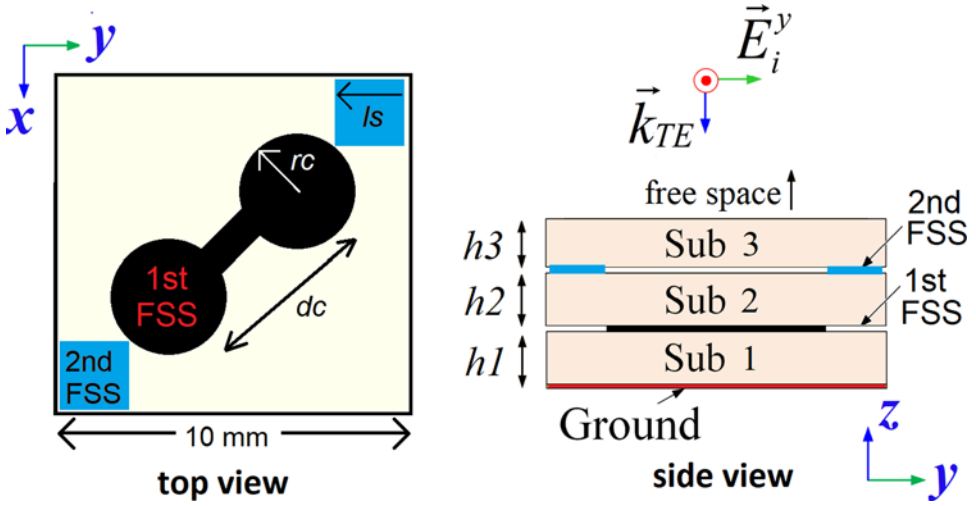


**Figure 1.** Configuration of the proposed reflective triple-layer dual-FSS-based LP–CP converter. CP = circularly polarized; FSS = frequency-selective structures; LP = linearly polarized.

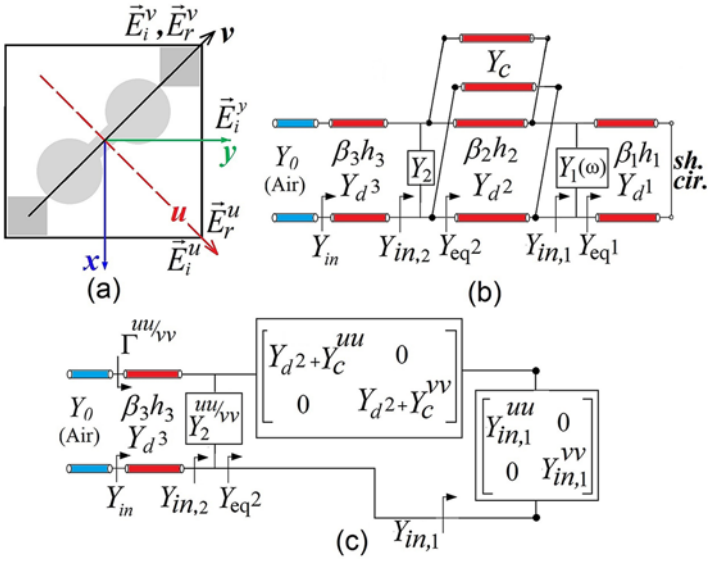


**Figure 2.** (a) Incident and reflective $u$ and $v$ orthogonal E field components of $y$-polarized incident wave. (b) Equivalent circuit model of the unit cell (***sh. cir.***: short circuit load). (c) Simplified model.

calculated by examining the shape and dimensions of the conductor surfaces and their discontinuities [32, 33]; and (2) Defining a mutual-coupling admittance, $Yc$, between FSS1 and FSS2 parallel to the transmission line between them, due to the possibility of their metal surfaces overlapping and changing total reflection characteristics.

In the analysis of the model based on Fig. 2(b), the first step is to calculate $Y_{eq}1$ using the expression $-jY_d1\,cot\,(\beta_1 h_1)$, where $Y_d i = Y_0/\sqrt{\varepsilon_r i}$ and $\beta_i = 2\pi\sqrt{\varepsilon_r i}/\lambda$ $(i = 1, 2, 3)$ [34]. $Y_{eq}1$ is assumed constant with respect to $u$ and $v$ polarizations, but $Y_1(\omega)$ is defined as a variable. These admittances are parallel, and their equivalent matrix is presented in Fig. 2(c) with the title of $Y_{in,1}^{uu/vv}$. Therefore, $Y_{in,1}^{uu} = -jY_d1\,cot\,(\beta_1 h_1) + Y_1{}^{uu}(\omega)$ and $Y_{in,1}^{vv} = -jY_d1\,cot\,(\beta_1 h_1) + Y_1{}^{vv}(\omega)$ are defined as final loads for each of the $u$ and $v$ polarizations, independently. Before these loads, the admittance of the second transmission line, $Y_d2$, is added to the polarization-dependent mutual-coupling admittance, $Y_C^{uu/vv}$, and results in an equivalent matrix as shown in Fig. 2(c). Here, the sum of these two admittances is defined as an equivalent characteristic admittance for each polarization, individually. Therefore, for the mentioned equivalent line and final loads, the input admittance $Y_{eq}2$ for each polarization is defined as follows [34]:

$$Y_{eq}^{uu/vv}2 = \left(Y_d2 + Y_C^{uu/vv}\right) \times \frac{\begin{array}{r} -jY_d1\,cot\,(\beta_1 h_1) + Y_1{}^{uu/vv}(\omega) \\ +j\left(Y_d2 + Y_C^{uu/vv}\right).tan\,(\beta_2 h_2) \end{array}}{\begin{array}{r} Y_d2 + Y_C^{uu/vv} \\ +j\left(-jY_d1\,cot\,(\beta_1 h_1) + Y_1{}^{uu/vv}(\omega)\right).tan\,(\beta_2 h_2) \end{array}} \quad (1)$$

According to Fig. 2(c), $Y_{eq}^{uu/vv}2$ is parallel to $Y_2^{uu/vv}$ corresponding to FSS2. Hence, $Y_{in,2}^{uu/vv} = Y_{eq}^{uu/vv}2 + Y_2^{uu/vv}$ is defined as the terminal loads of the third transmission line for each polarization independently. Again, we use the input admittance formula

https://doi.org/10.1017/S1759078723001629 Published online by Cambridge University Press

of a transmission line with characteristic admittance of $Y_d3$ with terminal load of $Y_{in,2}^{uu/vv}$ to calculate $Y_{in}^{uu/vv}$ as follows:

$$Y_{in}^{uu/vv} = Y_d3\,\frac{Y_{in,2}^{uu/vv} + jY_d3\,tan\,(\beta_3 h_3)}{Y_d3 + jY_{in,2}^{uu/vv}\,tan\,(\beta_3 h_3)} \tag{2}$$

Given the determination of $Y_{in}^{uu/vv}$at the position connected to air, it is necessary to calculate the reflection coefficients for both polarizations using $\Gamma^{uu/vv} = (Y_0 - Y_{in}^{uu/vv})/(Y_0 + Y_{in}^{uu/vv})$ [32]. As discussed in [34], the condition $\Gamma^{vv} = \mp j\Gamma^{uu}$ must be established to produce CP in reflected waves, where the upper or lower sign is used to have right-hand circularly polarization (RHCP) or left-hand circularly polarization (LHCP), respectively. To simplify the analysis, we assume the total losses to be close to zero, and then we can model the FSSs with pure imaginary shunt admittances as: ${Y_1}^{uu} = j{B_1}^{uu}$, ${Y_2}^{uu} = j{B_2}^{uu}$, ${Y_1}^{vv} = j{B_1}^{vv}$, and ${Y_2}^{vv} = j{B_2}^{vv}$. On the other hand, according to the direction defined for both FSSs (i.e., $v$ axis), ${B_1}^{uu}$, ${B_2}^{uu}$, and $Y_C^{uu}$ are generally very small due to minimal effective width along $u$-direction. Therefore, they are omitted for simplicity. In addition, considering the equality of dielectric constants for all layers, we have $Y_d1 = Y_d2 = Y_d3 = Y_d$ and $\beta_1 = \beta_2 = \beta_3 = \beta$. Finally, given that the third dielectric is considered only a thin and protective layer and its behavior toward both polarizations is the same, we can disregard it, and then, equation (2) becomes $Y_{in}^{uu/vv} = Y_{in,2}^{uu/vv}$. Based on these assumptions and simplifications and applying all mentioned relations in the CP condition (i.e., $\Gamma^{vv} = \mp j\Gamma^{uu}$), the required $v$-directed admittances of the FSSs will be [32]:

$$B_2{}^{vv} = \left[\frac{Y_{eq}^{uu}2 \mp jY_0}{Y_0 \mp jY_{eq}^{uu}2} - Y_{eq}^{vv}2\right] \text{ and } B_2{}^{uu} \cong 0, \tag{3}$$

where

$$Y_{eq}^{uu}2 = jY_d\left[\frac{tan\,(\beta h_2) - cot\,(\beta h_2)}{1 + tan\,(\beta h_2)\,cot\,(\beta h_2)}\right] \tag{4}$$

and

$$B_1{}^{vv} = Y_d cot\,(\beta h_1) - j(Y_d + Y_C^{vv})\frac{Y_{eq}^{vv}2 - j(Y_d + Y_C^{vv})tan\,(\beta h_2)}{(Y_d + Y_C^{vv}) - jY_{eq}^{vv}2\,tan\,(\beta h_2)} \text{ and } B_1{}^{uu} \cong 0. \tag{5}$$

According to the dielectric characteristics of the second layer, equation (4) can be calculated, and to determine equation (3), we need to determine the unknowns of equation (5). As another technique, if one value (e.g., $B_2{}^{vv}$) is taken as reference, then it will be possible to use equations (4) and (3) simultaneously to compute the corresponding required value of $Y_{eq}^{vv}2$. In the following, using equation (5), $B_1{}^{vv}$ is calculated. The method of obtaining certain values for $B_1{}^{vv}$and $B_2{}^{vv}$, based on the tensor surface impedance matrix and the corresponding physical parameters, has been reported in [32] and [33]. To determine $Y_C^{vv}$ in equation (5), another reference can be assumed based on the overlap of FSSs (i.e., the increase rate of $rc$ and $ls$ simultaneously) and the characteristics of the second dielectric.

As a result, it is proved that the degrees of freedom for the proposed design are high for great control over the number of reflection resonances, their overlap, the upper and lower edges of the conversion band, the conversion bandwidth, and the quality of the LP–CP conversion. The conversion quality is evaluated by the $AR$ parameter of the reflected waves for two polarizations, which is calculated as follows [34]:

$$AR = \left(\frac{|r_{xx}|^2 + |r_{yx}|^2 + \sqrt{XY}}{|r_{xx}|^2 + |r_{yx}|^2 - \sqrt{XY}}\right)^{1/2}, \tag{6}$$

where

$$XY = |r_{xx}|^4 + |r_{yx}|^4 + 2|r_{xx}|^2|r_{yx}|^2\cos\left(2\Delta\varphi_{xy}\right)$$

Here, $r_{xx}$ and $r_{yx}$ are the reflection coefficients of mutually orthogonal components, and $\Delta\varphi_{xy}$ is the phase difference between them. The condition of CP is $|r_{xx}| \cong |r_{yx}|$ and $\Delta\varphi_{xy} = \varphi_{xx} - \varphi_{yx} = 2m\pi \pm \frac{\pi}{2}$ simultaneously, where $m$ is an integer. In this paper, to have a high-quality conversion, the references are selected in such a way that we reach the target $AR$ below 2 dB.

## Parametric study, optimal results, and current distribution

In this section and according to the description presented on the circuit model, we will conduct a step-by-step analysis of the key parameters of FSS1 and FSS2, as well as the thickness of their dielectric covering, to investigate their effects on the upper and lower edges of the conversion band, reflective resonance number, overall 3 dB-$AR$ bandwidth, and $AR$ quality. We will be using HFSS software for parametric simulations and optimizations on both the single cell and final array, employing special boundary conditions, Master-Slave, under Floquet port excitation in both horizontal and vertical LPs. For our initial studies, we have chosen Rogers RT/duroid 5880 as dielectric material, with a dielectric constant of 2.2 and a loss tangent of 0.001. Here, the copper surfaces are assumed to be lossless. It is important to note that we have chosen a converter cell size of 10 mm × 10 mm, which is small enough compared to the highest frequency wavelength in the band to ensure accurate circuit analysis on the lumped cell. We have also set limits for certain physical parameters and will be conducting parametric studies within a reasonable range.

### Study on FSS1 and relevant dielectric

According to the theory mentioned above, FSS1 should have a multi-resonance behavior and provide a major contribution in covering a wide conversion band. Figure 3(a) and (b) shows the AR graphs of the proposed converter for different values of $rc$ and $dc$ in FSS1, respectively. It is noteworthy that FSS2 was not used in this study. From Fig. 3(a), it is quite clear that increasing the radius of the circular patches or $rc$ leads to the lowering of the initial resonance and finally reduces the lower edge of the band, according to 3 dB reference. Here, the lower edge of the band drops from 11 GHz to 6.2 GHz, which is very valuable and provides a significant increase in bandwidth. In addition, with the increase of $rc$, the number of resonances in higher positions increases and can be a factor in reducing the level of $AR$ in the high band. As shown in Fig. 3(b), if the distance of the circular patches (or $dc$) is large enough, the electrical length of the first resonance increases, and the lower edge of the band decreases significantly. Also, with the increase of $rc$, the frequency distance of band nulls ($AR$ with high value) increases from each other, and then, the bandwidth and conversion quality in the middle band increases. Based on Fig. 3, the strong influence of $rc$ and $dc$ on the conversion characteristics is clear. The next key parameter is the thickness of the FSS1 substrate, which will have a significant effect on the effective dielectric

https://doi.org/10.1017/S1759078723001629 Published online by Cambridge University Press

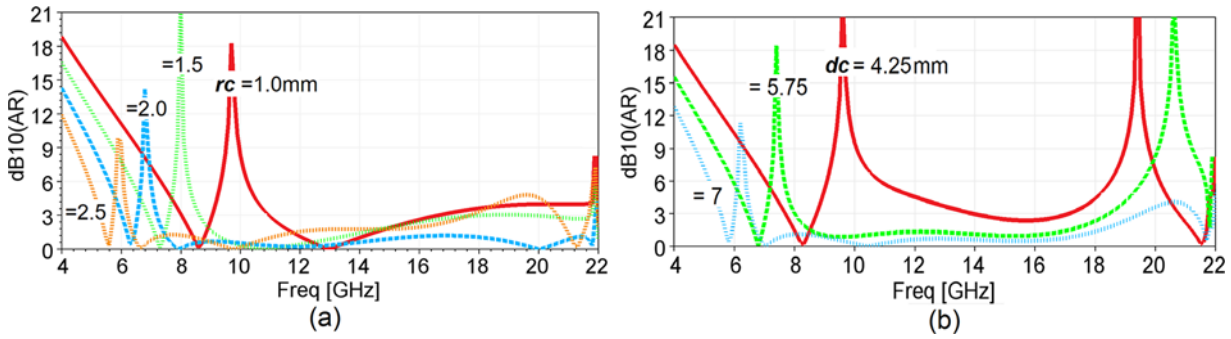


**Figure 3.** *AR* graphs (normal incident) of the proposed LP–CP converter (without FSS2) for different values of (a) $rc$ (when $dc$=7 mm and $h1$=1.55 mm) and (b) $dc$ (when $rc$=2.5 mm and $h1$=1.55 mm) in FSS1. AR = axial ratio; CP = circularly polarized; FSS = frequency-selective structures; LP = linearly polarized.

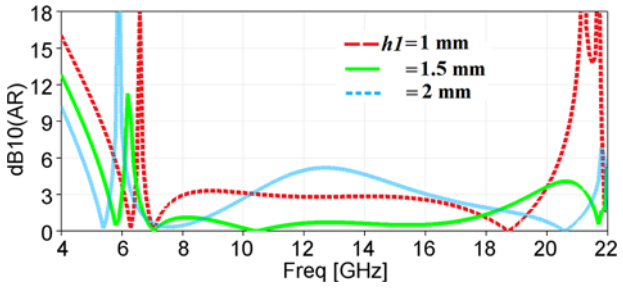


**Figure 4.** *AR* graphs (normal incident) of the proposed LP–CP converter (without FSS2) for different values of $h1$ in FSS1 (when $dc$=7 mm and $rc$=2.5 mm). AR = axial ratio; CP = circularly polarized; FSS = frequency-selective structures; LP = linearly polarized.

constant and the quality factor of most resonances. The result of the study is presented in Fig. 4. By controlling $h1$, the resonance of the first band moves down to some extent, and most importantly, the overlapping quality of the resonances in the middle band increases significantly. The relative reduction of the lower edge of the band and very high improvement of *AR* in the middle band are the results of this change. Simultaneous optimization of these parameters is required.

### Study on FSS2 and relevant dielectric

As discussed in the theory section, FSS2 is used to create high resonance and thus increase the bandwidth and improve the conversion quality from the upper edge of the band. The position of the square patches of FSS2 is fixed relative to the corners of the cell, and its dimensions (i.e., *ls*) increase toward the center of the cell; the results of which are presented in Fig. 5(a). It is important to note that altering *ls* can impact the field coupling between FSS2 and FSS1, potentially leading to changes in the quality factor and bandwidth of high resonances. It is quite clear that *ls* controls the high resonance position. By choosing values around 1.5 mm, not only the high resonance is at its highest position at around 20.8 GHz, but also the *AR* quality at the top of the band from 15 GHz onward is greatly increased. In the best case, the range of 6.2–21.2 GHz is covered with an *AR* of approximately less than 1.8 dB, which is the outcome of the simultaneous use of two FSSs, multi-resonance and single-high-resonance ones, at independent heights and positions.

The thickness of the substrate below FSS2 is equal to $h1+h2$. As illustrated in Fig. 5(b), this parameter can be effective partly in the position of high resonance and relevant *AR* quality, which should be involved in the optimization process.

### Parametric study on angular stability, dielectric constant analysis, and optimal results

At first, the incident angle is changed from 0° to 45°, and the 3 dB-*AR* bandwidths are calculated for the changes in the three key parameters of the converter. The relevant data are summarized in Table 1 for better comparison and study based on angular stability. It should be noted that the related graphs are not presented due to their large number and volume so as not to occupy more space. This table implies that the angular stability is maintained for the optimal values of the parameters more than the other values. In other words, the amount of bandwidth loss for increasing the incident angle is less when the parameter is at its optimal value. This result also exhibits the optimal number of parameters in terms of angular stability.

As a second study, the dielectric constant of all dielectrics changes within a reasonable range (1–6), so that its effects on the effective dielectric constant, the electrical length of the resonances, and the bandwidth are determined. The related *AR* results are shown in Fig. 6. Their properties are summarized in Table 2. According to Fig. 6, it is known that by increasing the dielectric constant and adjusting the quality factor of the resonances, the bandwidths decrease and the resonances overlap in a more limited range at lower frequencies. In addition, as the dielectric constant increases, the lower edge of the band is significantly reduced from 7.2 to 3.65 GHz. This ultimately results in a wider bandwidth of over 116% and, importantly, covers a portion of the standard S band. It is expected that by increasing the dielectric constant to 8, the entire S band (2–4 GHz) will be covered.

Given the large number of degrees of freedom in the design, a meticulous optimization process was conducted in the final stage, simultaneously considering all effective parameters within their logical ranges. Table 3 provides the optimal values, and then the total thickness of the cell (i.e., $h1+h2+h3$) is calculated to be equal to 3.2 mm (i.e., 0.06$\lambda$ @ 6 GHz). The graphs of the optimal cell are presented in Fig. 7. According to Fig. 7(a), 3 dB-*AR* bandwidth is 111.2% (6.12–21.42 GHz), while an excellent *AR* of less than 1.7 dB is obtained from 6.3 to 21 GHz (BW = 107%). As clearly seen from Fig. 7(b), the amplitude condition for having CP mode (i.e., $|r_{xx}| \cong |r_{yx}|$) is met from 6 to 21 GHz. As expected, their phase difference, $\Delta\varphi_{xy}$ (i.e., $\varphi_{xx}-\varphi_{yx}$) is shown in Fig. 7(c), which is around $-\frac{\pi}{2}$ or $+\frac{3\pi}{2}$, indicating the production of only RHCP mode in

https://doi.org/10.1017/S1759078723001629 Published online by Cambridge University Press

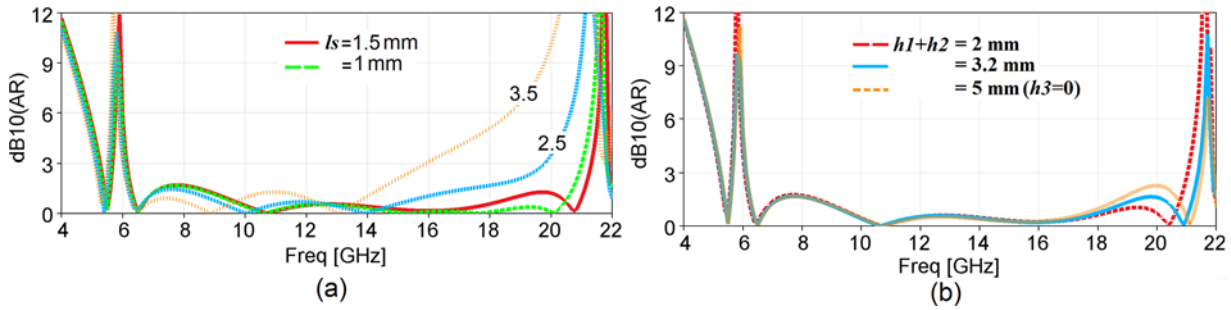


**Figure 5.** *AR* graphs (normal incident) of the proposed LP–CP converter (with FSS1) for different values of (a) *ls* and (b) $h1+h2$ in FSS2 (when $dc$=7 mm, $rc$=2.5 mm, and $h1$=1.55 mm). AR = axial ratio; CP = circularly polarized; FSS = frequency-selective structures; LP = linearly polarized.

**Table 1.** 3dB-*AR* bandwidths for different values of the parameters ($rc$, $dc$, and $ls$) versus different incident angles (BW: bandwidth)

| Parameters | *rc* | | | | *dc* | | | *ls* | | | |
|---|---|---|---|---|---|---|---|---|---|---|---|
| Parameter values (mm) | 1 | 1.5 | 2 | 2.5 | 4.25 | 5.75 | 7 | 1 | 1.5 | 2.5 | 3.5 |
| **3 dB-*AR* BW (Incident angle = 0°)** | 37% | 73% | 103% | 100% | 25% | 77% | 99% | 110% | 111% | 107% | 91% |
| **3 dB-*AR* BW (Incident angle = 15°)** | 34% | 71% | 101% | 99% | 22% | 75% | 98% | 89% | 91% | 88% | 86% |
| **3 dB-*AR* BW (Incident angle = 30°)** | 30% | 66% | 93% | 95% | 18% | 72% | 90% | 83% | 85% | 80% | 75% |
| **3 dB-*AR* BW (Incident angle = 45°)** | 19% | 58% | 73% | 77% | 8% | 60% | 78% | 70% | 78% | 66% | 60% |

AR = axial ratio.

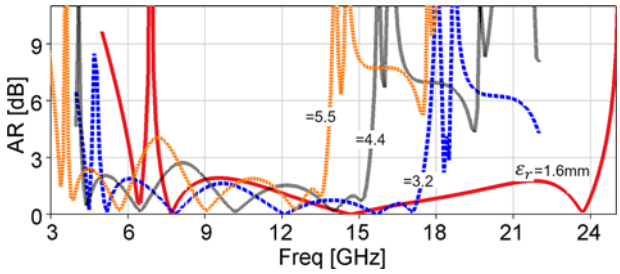


**Figure 6.** *AR* graphs for different dielectric constants for all layers simultaneously. AR = axial ratio.

the entire band. Another qualitative parameter is the polarization conversion efficiency (*PCE*), which is calculated as follows [3, 29]:

$$PCE = \frac{\left|r_{RHCP-j}\right|^2}{\left|r_{RHCP-j}\right|^2 + \left|r_{LHCP-j}\right|^2} \quad (j = x, y) \tag{7}$$

where the expressions related to right- and left-handed circular polarizations are

$$\begin{cases} r_{RHCP-j} = \dfrac{\sqrt{2}(r_{yj} + ir_{xj})}{2} \\ r_{LHCP-j} = \dfrac{\sqrt{2}(r_{yj} - ir_{xj})}{2} \end{cases} \quad (j = x, y). \tag{8}$$

Based on equations (7) and (8), *PCE, RHCP,* and *LHCP* are calculated, which are presented in Fig. 7(d) and (e), respectively. An excellent conversion efficiency of over 95% is achieved from 6.2 to 21.2 GHz. As shown in Fig. 7(e), there is a high purity between *RHCP* and *LHCP* modes. Moreover, *RHCP* amplitude ripple is very low in the entire band, which proves low conversion loss. It should be noted that due to the diagonal symmetry of FSSs, the results will be the same for *x*- and *y*-polarized incident waves, and so it is not necessary to repeat the results.

### Current distribution and CP validation

To fully comprehend the LP to CP conversion mechanism, it is crucial to investigate the surface current distributions on both the top and bottom surfaces of the cell at the desired frequencies with minimum *AR*. Figure 8 illustrates the results for four specific resonances. It is worth noting that for all resonances and on both upper and lower surfaces, all current vectors are aggregated, and the equivalent current vector (Jeq) is provided, as shown in the figure. It is evident that the equivalent currents in the upper and lower surfaces are perpendicular to each other, which is the primary condition for creating CP, while simultaneously stimulating a 90° phase difference between them. Based on Fig. 8(a) and (b), long and uniform currents are generated along the FSS1 diagonal, which is a contributing factor to creating high-efficiency reflective resonances at low frequencies. As depicted in Fig. 8(c), at 15.3 GHz, the edges of the circular patches are also activated, which creates

**Table 2.** *AR* properties of the proposed converter for different values of dielectric constants (according to Figure 6)

| Dielectric constant (for all layers simultaneously) | 1.6 | 2.2 | 3.2 | 4.4 | **5.5** |
|---|---|---|---|---|---|
| **Lower-edge frequency of 3 dB-*AR* band (GHz)** | 7.2 | 6.12 | 4.9 | 4.2 | 3.65 |
| **3 dB-*AR* bandwidth (GHz)(By %)** | 7.2 ~ 24.5(109) | 6.12 ~ 21.42(111.2) | 4.9 ~ 17.6(113) | 4.2 ~ 15.4(114.2) | 3.65 ~ 13.75(116.2) |

AR = axial ratio.

https://doi.org/10.1017/S1759078723001629 Published online by Cambridge University Press

**Table 3.** Optimal values of the parameters

| Parameters | *rc* | *dc* | *ls* | *h*1 | *h*2 | *h*3 |
|---|---|---|---|---|---|---|
| **Value (mm)** | 2.52 | 7 | 1.6 | 1.55 | 1.25 | 0.4 |

a shorter electrical length and slightly tilts the direction of Jeq. According to Fig. 8(d), two patches of FSS2 are activated, perpendicular to ground current. It should be noted that at this frequency, the current distribution on FSS1 is highly irregular and therefore will not be effective in reflecting the wave. We have not included the related graph for brevity. Lastly, it is important to mention that we examined the current distributions for both *x*- and *y*-directed incident waves, and the results were quite similar. Therefore, we do not present them here for brevity.

## Fabrication, measurement, and comparison

A prototype was implemented to verify the proposed converter design, as shown in Fig. 9(a), including photographs of FSS1 and FSS2 layers. The sample consists of 8 × 8 cells for FSS1 and FSS2 layers, both etched in an area of 80 mm × 80 mm on the Rogers RT/duroid 5880 substrates. It is mentioned that to use the standard thicknesses in the manufacturing process, the laminates with thicknesses of 1.575 mm, 0.5 mm, and 0.78 mm were used and carefully combined, respectively.

Next, suitable laminates are carefully placed on top of each other and stick together. Compared to the optimal thicknesses in Table 3, there is a slight difference that can be overlooked. A measurement setup was built as illustrated in Fig. 9(b). Two broadband rectangular standard horn antennas with small aperture were connected to the Agilent E8361A-VNA (10 MHz–67 GHz). Limited to the frequency range of the VNA, we only managed and calibrated it to measure the *AR* in the range of 3–23 GHz. To increase the accuracy of the measurement, the distance between the sample and the antennas was chosen to be greater than $2D^2/\lambda$ (100 cm for $\lambda$ at 22 GHz), and the ground plane at the bottom of the sample was determined as the measurement reference. For near-field isolating between the horn apertures, a thin absorber was used between them. Also, some pyramidal EM absorbers were employed behind the sample and around it to eliminate reflections. For $r_{xx}$ measurement, the direction of the receiver was constant and for $r_{yx}$ one, the receiving horn was rotated by 90°. In this way, and using equation (6), the *AR* can be calculated. This process is repeated for four different incident angles ($\theta = 0°, 15°, 30°, 45°$) and the relevant *AR*s are shown in Fig. 10. For all angles, a good agreement between simulation and measurement is observed. It is seen that 3 dB-*AR* bandwidth becomes smaller as the incidence angle increases. For angle deviation up to 45°, the CP bandwidth is maintained at 78%

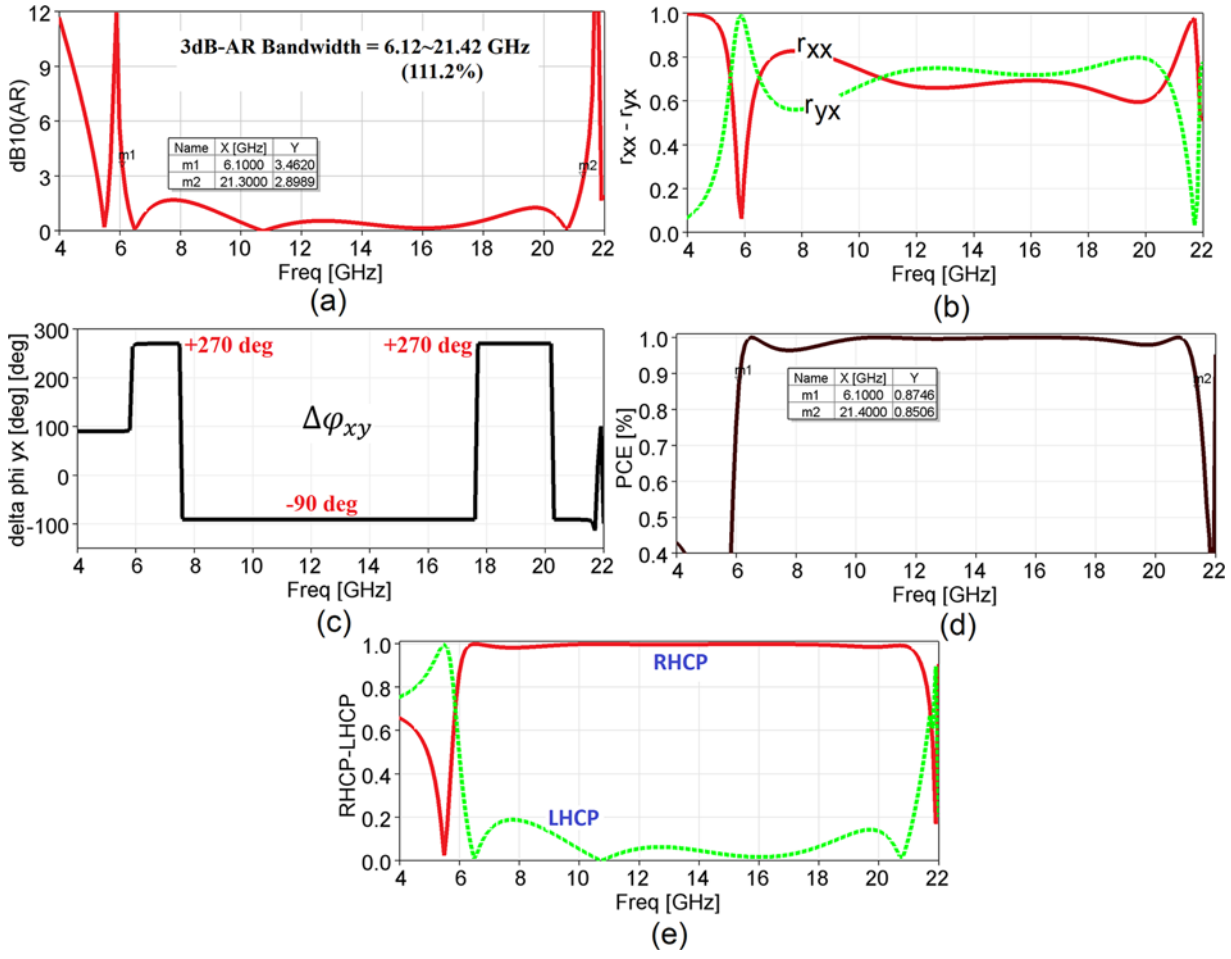


**Figure 7.** Optimal results including: (a) *AR*, (b) reflection coefficients, (c) reflection phase difference, (d) *PCE*, and (e) polarization mode. AR = axial ratio; PCE = polarization conversion efficiency.

https://doi.org/10.1017/S1759078723001629 Published online by Cambridge University Press

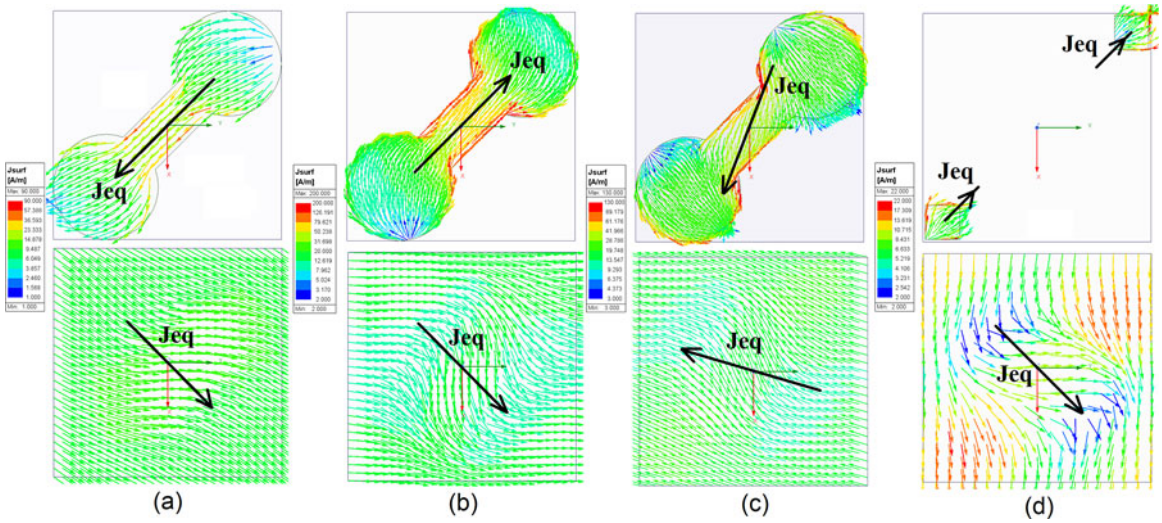


**Figure 8.** Current distributions on top (FSS1 and FSS2) and bottom (ground plane) layers at resonances with minimum $AR$: (a) 6.5 GHz, (b) 10.7 GHz, (c) 15.3 GHz, and (d) 20.1 GHz. AR = axial ratio; FSS = frequency-selective structure.

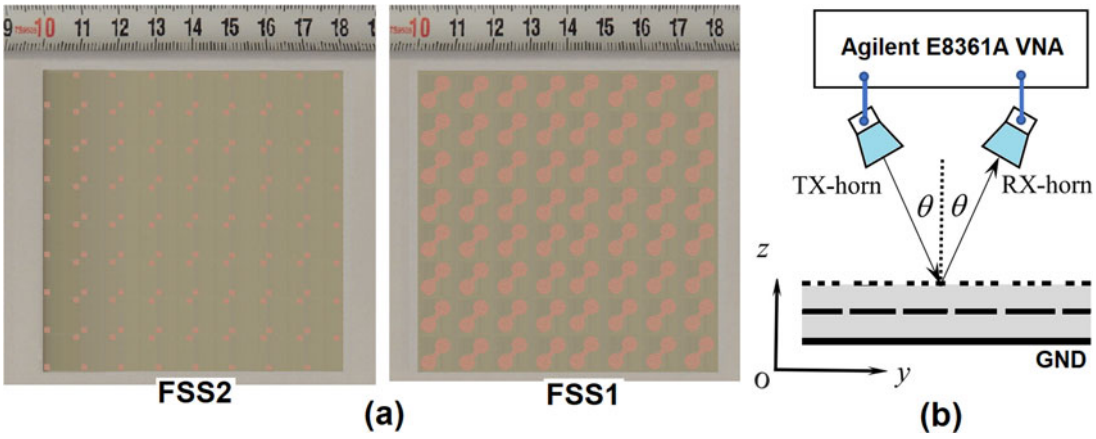


**Figure 9.** (a) Photographs of the fabricated prototype (FSS1 and FSS2) and (b) measurement setup. FSS = frequency-selective structure.

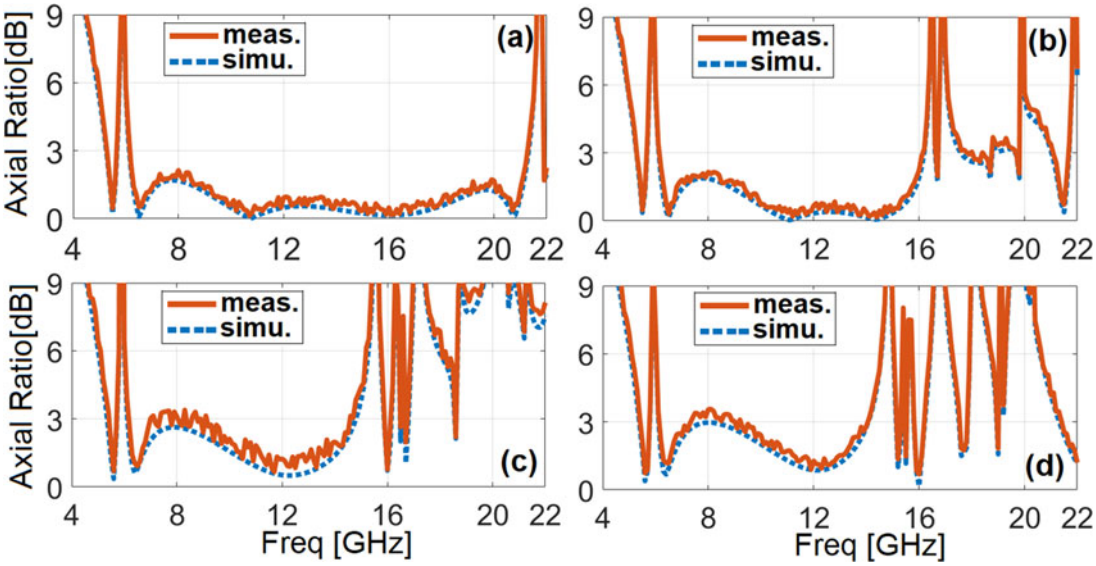


**Figure 10.** Measured and simulated axial ratio versus frequency for different incident angles: (a) $\theta = 0^\circ$, (b) $\theta = 15^\circ$, (c) $\theta = 30^\circ$, and (d) $\theta = 45^\circ$.

https://doi.org/10.1017/S1759078723001629 Published online by Cambridge University Press

**Table 4.** Comparison between proposed work and some existing LP–CP reflective converters (**: this work, and BW: bandwidth)

| Reference | [31] | [28] | [25] | [23] | [21] | [9] | [7] | [6] | [5] | [3] | [2] | [1] | ** |
|---|---|---|---|---|---|---|---|---|---|---|---|---|---|
| **Metal layers** | 1 | 5 | 4 | 1 | 2 | 2 | 6 | 4 | 2 | 1 | 1 | 2(2 vias) | 2 |
| **3 dB-*AR* BW** | 50% | 20% | 37% | 47% | 42% | 55% | 40% | 64% | 24% | 95% | 46% | 128% | 109–116% |
| **Thickness ($\times\lambda_0$)** | 0.035 | 1.08 | 0.83 | 0.02 | 0.48 | 0.13 | 0.18 | 0.17 | 0.27 | 0.08 | 0.05 | 0.308 | 0.039 |
| **Angle stability** | $< 45^\circ$ | 50° | 25° | 30° | 20° | 55° | 45° | 20° | 60° | – | 30° | 10° | 45°BW:78% |

CP = circularly polarized; LP = linearly polarized

(6.15–14.1 GHz), which indicates an angular stability, covering C, X, and Ku standard bands.

A comparison between the proposed work and the other reflective converters is shown in Table 4. It can be observed that the highest bandwidth is obtained for a structure with high thickness and two vias [1]. Reflective converters with four or more layers have high thickness and bandwidth below 65% [6, 7, 25, 28]. Reference [3] is a good sample that has achieved high bandwidth despite being a single layer with low thickness. Among designs with two layers without short-circuited vias, our proposed converter has low thickness of less than $0.04\lambda_0$ at 3.65 GHz and a very high bandwidth of over 109%. Finally, by comparing the angular stability and 3dB-CP bandwidth coverage for the presented converter and other references and for the deviation of the radiation angle up to 45°, the bandwidth in our design is maintained at about 78%, which is a better characteristic than many references. It is clear from the data in the table that the higher bandwidth [1] is achieved at the same time as the very low angular stability, which is itself a limitation. Similarly, as the covered incident angle [5, 9, 28] increases, the bandwidth drops drastically.

## Conclusion

A wideband thin LP–CP converter has been realized using a stacked structure of two FSS layers with array structures of square patches and multi-resonance interconnected circular patches. The high overlap of several resonances resulted in a very low *AR* in the entire bandwidth above 110%, which indicates a high conversion efficiency. In addition, circuit-admittance modeling with high degree of freedom was presented, and the unknowns required for the physical design of both FSSs were presented as closed-form equations. Controlling the CP frequency bandwidth, and angular stability up to 45° with a 78% bandwidth have been also proven.

**Competing interest.** The authors declare that they have no known competing financial interests or personal relationships that could have appeared to influence the work reported in this paper. It is also added that the authors of this article do not have any financial support from the university or personally.

## References

1. **Jia Y, Liu Y, Zhang W, Wang J, Wang Y, Gong S and Liao G** (2018) Ultra-wideband metasurface with linear-to-circular polarization conversion of an electromagnetic wave. *Optical Materials Express* **8**, 597–604.
2. **Kundu D, Singh J, Singh D and Chakrabarty A** (2021) Design and analysis of broadband ultrathin reflective linear-to-circular polarization converter using polygon-based anisotropic-impedance surface. *IEEE Transactions on Antennas and Propagation* **69**, 5154–5159.
3. **Lin B, Guo J, Lv L, Wu J, Ma Y, Liu B and Wang Z** (2019) Ultra-wideband and high-efficiency reflective polarization converter for both linear and circular polarized waves. *Applied Physics* **76**, 1–8.
4. **Liu X, Zhou Y, Wang C, Gan L, Yang X and Sun L** (2022) Dual-band dual-rotational-direction angular stable linear-to-circular polarization converter. *IEEE Transactions on Antennas and Propagation* **70**, 6054–6059.
5. **Arnieri E, Greco F and Amendola G** (2021) A broadband, wide-angle scanning, linear-to-circular polarization converter based on standard Jerusalem cross frequency selective surfaces. *IEEE Transactions on Antennas and Propagation* **69**, 578–583.
6. **Zhang W, Li J-Y and Xie J** (2017) A broadband circular polarizer based on cross-shaped composite frequency selective surfaces. *IEEE Transactions on Antennas and Propagation* **65**, 5623–5627.
7. **Momeni Hasan Abadi SMA and Behdad N** (2016) Wideband linear-to-circular polarization converters based on miniaturized-element frequency selective surfaces. *IEEE Transactions on Antennas and Propagation* **64**, 525–534.
8. **Tao X, Qi L, Yang J, Uqaili JA, Lan F and Yang Z** (2023) Bifunctional terahertz metasurface for transmissive broadband linear-to-circular and linear polarization conversion. *IEEE Transactions on Terahertz Science and Technology* **13**, 254–261.
9. **Wang HB, Cheng YJ and Chen ZN** (2020) Wideband and wide-angle single-layered substrate linear-to-circular polarization metasurface converter. *IEEE Transactions on Antennas and Propagation* **68**, 1186–1191.
10. **Wang J, Jin C, Jiang YN and Chen YJ** (2023) A terahertz wideband linear-to-circular polarization converter based on meandering-structured metasurface. *Optics Communications* **548**, 129876.
11. **Nan L, Jingcheng Z, Peiyi T and Yongzhi C** (2023) Broadband and high-efficient reflective linear–circular polarization convertor based on three-dimensional all-metal anisotropic metamaterial at terahertz frequencies. *Optics Communications* **541**, 129544.
12. **Zaker R and Sadegzadeh A** (2019) A low-profile design of polarization rotation reflective surface for wideband RCS reduction. *IEEE Antennas and Wireless Propagation Letters* **18**(9), 1794–1798.
13. **Zaker R and Sadeghzadeh A** (2018) Double-layer ultra-thin artificial magnetic conductor structure for wideband radar cross-section reduction. *IET Microwaves, Antennas & Propagation* **12**(9), 1601–1607.
14. **Zaker R and Sadeghzadeh A** (2018) Wideband radar cross section reduction using a novel design of artificial magnetic conductor structure with a triple-layer chessboard configuration. *International Journal of RF and Microwave Computer-Aided Engineering*, **29**(2), e21545.
15. **Zaker R and Sadeghzadeh A** (2020) Passive techniques for target radar cross section reduction: A comprehensive review. *International Journal of RF and Microwave Computer-Aided Engineering* **30**(11), e22411.
16. **Arbabi A, Horie Y, Bagheri M and Faraon A** (2015) Dielectric metasurfaces for complete control of phase and polarization with subwavelength spatial resolution and high transmission. *Nature Nanotechnology* **10**, 937–943.
17. **Zhang W, Li B and Zhu L** (2023) Orthogonal adjacent-order filtering element-based wideband transmissive linear-to-circular polarization converter. *IEEE Transactions on Antennas and Propagation* **71**, 3324–3334.
18. **Fonseca Dias LF, Jouvaud C, Delaveaud C and Aubert H** (2022) Antenna loading by passive impedance for linear-to-circular polarization conversion. *IEEE Antennas and Wireless Propagation Letters* **21**, 1892–1895.
19. **Bhattacharjee A and Dwari S** (2022) Design of an anisotropic reconfigurable reflective polarization converter for realizing circular polarization-reconfigurable antenna. *IEEE Antennas and Wireless Propagation Letters* **21**, 2392–2396.

https://doi.org/10.1017/S1759078723001629 Published online by Cambridge University Press

20. **Sofi MA, Saurav K and Koul SK** (2022) Linear-to-circular polarization converter with wide angular stability and near unity ellipticity, application to linearly polarized antenna array. *IEEE Transactions on Circuits and Systems II* **69**, 4779–4783.
21. **Li HX, Li B and Zhu L** (2019) Wideband linear-to-circular polarizer based on orthogonally inserted slot line structures. *IEEE Antennas and Wireless Propagation Letters* **18**, 1169–1173.
22. **Chen Y, Zhai G, Wang S, Gao J and Ren J** (2023) Dual-band single-layered linear-to-dual-circular polarization converter with high angle stability for satellite communication. *IEEE Antennas and Wireless Propagation Letters* **22**, 2017–2021.
23. **Fei P, Shen Z, Wen X and Nian F** (2015) A single-layer circular polarizer based on hybrid meander line and loop configuration. *IEEE Transactions on Antennas and Propagation* **63**, 4609–4614.
24. **Dicandia FA and Genovesi S** (2022) Linear-to-circular polarization transmission converter exploiting meandered metallic slots. *IEEE Antennas and Wireless Propagation Letters* **21**, 2191–2195.
25. **Lourdes ML, Jorge RC and Jose IML** (2014) A multilayer circular polarizer based on bisected split-ring frequency selective surfaces. *IEEE Antennas and Wireless Propagation Letters* **13**, 153–156.
26. **Zixiang L, Ruipeng L, Xia W, Hongxing Z, Mengjun W and Erping L** (2020) Metasurface: Changing polarization from linear to circular for airborne antenna. *AEU – International Journal of Electronics and Communications* **116**, 153086.
27. **Xiao-Feng L, Guang-Ming W, Xiao-Jun Z, Tang-Jing L and Tong C** (2023) Broadband circularly polarized folded transmitarray antenna based on polarization conversion metasurfaces. *AEU – International Journal of Electronics and Communications* **163**, 154596.
28. **Blanco D and Sauleau R** (2018) Broadband and broad-angle multilayer polarizer based on hybrid optimization algorithm for low-cost Ka-Band applications. *IEEE Transactions on Antennas and Propagation* **66**, 1874–1881.
29. **Zhang BM, Zhu CH, Zhang R, Yang XF, Wang Y and Liu XM** (2022) Dual-band wide-angle reflective circular polarization converter with orthogonal polarization modes. *Sensors* **22**, 9728.
30. **Shukoor MA and Dey S** (2022) Novel miniaturized arrow linked figure of eight square loop FSS-based multiband linear-circular and linear-cross reflective microwave polarizer. *International Journal of Microwave and Wireless Technologies* **15**, 591–599.
31. **Shukoor MA and Dey S** (2023) Highly miniaturized wideband angular stable linear–circular and linear–cross polarization converter for Ka-band satellite applications. *International Journal of Microwave and Wireless Technologies* **15**, 1557–1569.
32. **Doumanis E, Goussetis G, Gomez-Tornero JL, Cahill R and Fusco V** (2012) Anisotropic impedance surfaces for linear to circular polarization conversion. *IEEE Transactions on Antennas and Propagation* **60**, 212–219.
33. **Lee J and Sievenpiper DF** (2019) Method for extracting the effective tensor surface impedance function from nonuniform, anisotropic, conductive patterns. *IEEE Transactions on Antennas and Propagation* **67**, 3171–3177.
34. **Balanis CA** (1999) *Advanced Engineering Electromagnetics*. India: Wiley.


**Reza Zaker** was born in Tabriz, Iran, in 1982. He received the MSc degree in Electrical and Telecommunication Engineering from Urmia University, Urmia, Iran, in 2008, and a PhD degree in Electrical Engineering at Amirkabir University of Technology, Tehran, Iran, in 2014. He is an associate professor in the Department of Electrical Engineering, Azarbaijan Shahid Madani University, Tabriz, Iran. He is a reviewer for IEEE and IET journals in Antenna and Microwave fields. He has authored or co-authored several refereed journal articles and local and international conference papers. His research areas include MIMO antennas, phased array antenna, anti-radar and polarization converter structure design, meta-material, reconfigurable antenna, RF/ microwave/mm-wave circuit, and nonlinear modeling.

**Farid Jolani** was born in Tabriz, Iran, in 1991. He received the BSc degree in Electrical and Telecommunication Engineering from Tabriz University, Tabriz, Iran, and the MSc degree in Electrical and Telecommunication Engineering (Fields and Waves) from Azarbaijan Shahid Madani University, Tabriz, Iran. His research areas include frequency-selective structures, metasurfaces, and polarization converters.

https://doi.org/10.1017/S1759078723001629 Published online by Cambridge University Press